Faraday Discussions

Cite this: *Faraday Discuss.*, 2023, **245**, 261

PAPER

Experimental, theoretical, and astrochemical modelling investigation of the gas-phase reaction between the amidogen radical (NH_2) and acetaldehyde (CH_3CHO) at low temperatures†

Kevin M. Douglas, *[a] Lok Hin Desmond Li, [a] Catherine Walsh, [b] Julia H. Lehman, [c] Mark A. Blitz [ad] and Dwayne E. Heard *[a]

Received 20th February 2023, Accepted 30th March 2023
DOI: 10.1039/d3fd00046j

The first experimental study of the low-temperature kinetics of the gas-phase reaction of NH_2 with acetaldehyde (CH_3CHO) has been performed. Experiments were carried out using laser-flash photolysis and laser-induced fluorescence spectroscopy to create and monitor the temporal decay of NH_2 in the presence of CH_3CHO. Low temperatures relevant to the interstellar medium were achieved using a pulsed Laval nozzle expansion. Rate coefficients were measured over the temperature and pressure range of 29–107 K and 1.4–28.2 $\times$ 10^{16} molecules per cm^3, with the reaction exhibiting a negative temperature dependence and a positive pressure dependence. The yield of CH_3CO from the reaction has also been determined at 67.1 and 35.0 K, by observing OH produced from the reaction of CH_3CO with added O_2. *Ab initio* calculations of the potential energy surface (PES) were combined with Rice–Rampsberger–Kessel–Marcus (RRKM) calculations to predict rate coefficients and branching ratios over a broad range of temperatures and pressures. The calculated rate coefficients were shown to be sensitive to the calculated density of states of the stationary points, which in turn are sensitive to the inclusion of hindered rotor potentials for several of the vibrational frequencies. The experimentally determined rate coefficients and yields have been used to fit the calculated PES, from which low-pressure limiting rate coefficients relevant to the ISM were determined. These have been included in a single-point dark cloud astrochemical model, in which the reaction is shown to be a potential source of gas-phase CH_3CO radicals under dark cloud conditions.

[a]*School of Chemistry, University of Leeds, Leeds, LS2 9JT, UK. E-mail: k.m.douglas@leeds.ac.uk; d.e.heard@leeds.ac.uk*
[b]*School of Physics and Astronomy, University of Leeds, Leeds, LS2 9JT, UK*
[c]*School of Chemistry, University of Birmingham, Edgbaston, B15 2TT, UK*
[d]*National Centre for Atmospheric Science (NCAS), University of Leeds, Leeds, LS2 9JT, UK*

† Electronic supplementary information (ESI) available. See DOI: https://doi.org/10.1039/d3fd00046j

1. Introduction

An active field of astrochemical research remains the understanding of the reaction mechanisms for the formation of complex organic molecules (COMs), which are molecules observed in space containing carbon with at least 6 atoms.[1] Since the early 1960s, the development of ground based radio astronomy has led to a rapid rate of detection of COMs with a wide range of functional groups in the interstellar medium (ISM).[2] The detection of COMs at very high spatial resolution in cold objects suggests a gas-phase route to their formation rather than just *via* a pure surface-grain chemistry mechanism.[3] However, the mechanisms for forming many gas-phase COMs are still unknown, with both gas-phase and grain-surface (*via* non-thermal desorption) routes possible.

The formation of biomolecules such as amino acids from COMs under prebiotic conditions has attracted much interest.[4] Amino acids such as glycine (NH_2CH_2COOH), which has been observed in the coma of a comet,[5] are building blocks for proteins, which are essential components of all living systems. The peptide bond (NH–C═O) the plays a key role in the linking of amino acids into peptide chains and proteins, and contains all the components necessary for the formation of nucleic polymers under prebiotic conditions.[6] However, only two molecules containing this bond have been observed in space, formamide (NH_2CHO),[7] and acetamide ($NH_2C(O)CH_3$).[8]

In a previous paper[9] we investigated the low-temperature kinetics of the gas-phase reaction between the amidogen radical (NH_2) and formaldehyde (CH_2O) as a possible source of interstellar formamide. In this paper, we have performed an experimental and theoretical study of the kinetics of the reaction of NH_2 with acetaldehyde, the next aldehyde in the homologous series after formaldehyde, for which there are three energetically favourable channels (ΔH calculated in this study, see Section 4):

$$NH_2 + CH_3CHO \rightarrow NH_3 + CH_3CO, \quad \Delta H^\circ_{0\ K} = -72 \ \left(\text{kJ mol}^{-1}\right) \qquad \text{(R1a)}$$

$$NH_2 + CH_3CHO \rightarrow NH_3 + CH_2CHO, \quad \Delta H^\circ_{0\ K} = -43 \ \left(\text{kJ mol}^{-1}\right) \qquad \text{(R1b)}$$

$$NH_2 + CH_3CHO \rightarrow NH_2COCH_3 + H, \quad \Delta H^\circ_{0\ K} = -30 \ \left(\text{kJ mol}^{-1}\right) \qquad \text{(R1c)}$$

Reaction (R1) therefore, is both a potential source of gas-phase organic radicals (CH_3CO and CH_2CHO *via* reactions (R1a) and (R1b), respectively), and of acetamide (NH_2COCH_3, *via* reaction (R1c)), the largest interstellar molecule with a peptide bond that has so far been observed in space.[8] We present measurements of rate coefficients for the reaction of NH_2 and CH_3CHO in the range 29–107 K, using a pulsed laser photolysis-laser induced fluorescence (PLP-LIF) technique coupled with a Laval nozzle to achieve the low temperatures relevant to the ISM. We also report an experimental measurement of the absolute branching yield for reaction (R1a) generating NH_3 + CH_3CO products at 35 K and 67 K. We also performed a theoretical investigation of the reaction using *ab initio* methods to calculate the potential energy surface, and used reaction rate theory to calculate both rate coefficients and product branching ratios over the temperature range 20–400 K. These kinetic data are then incorporated into a single point dark cloud

astronomical model to assess the impact of the newly determined rate coefficients. A more detailed introduction to the low-temperature kinetics of gas-phase reactions, to the astrochemistry of acetamide, and to the related reaction between NH_2 and formaldehyde, is given in the ESI in Section S1.†

2. Methodology

2.1 Experimental study

The use of a Laval nozzle expansion coupled with a PLP-LIF technique has been employed by this group to study a range of low temperature neutral–neutral reactions, including reactions of OH with unsaturated hydrocarbons[10] and VOCs,[11–14] $^1CH_2$ (singlet methylene) with atmospheric gases and hydrocarbons,[15,16] CH with CH_2O,[17] and NH_2 with CH_2O.[9] In the current study, we employ the same technique to study the low temperature reaction of NH_2 with CH_3CHO. As the experimental apparatus employed in the current and previous studies has been discussed in detail elsewhere,[10–13] only a very brief overview is given here, with additional details given in the ESI in Section S2.†

The low temperatures employed in this study were obtained by the isentropic expansion of a gas mixture from a high pressure reservoir to a low pressure chamber through a Laval nozzle, producing a thermalized low temperature gas flow that is stable for several centimetres from the nozzle exit. A set of 4 nozzles were used during the experiments to achieve flow temperatures of between 29 and 107 K. The density and temperature profile of the flows were characterized by impact pressure measurements, and the temperature of several of the uniform flows was confirmed by rotationally resolved LIF spectroscopy.[15,17]

The gas mixture introduced to the reservoir consists primarily of an inert bath gas (Ar (99.9995%, BOC), He (99.9995%, BOC), or N_2 (99.9995%, BOC)), together with smaller amounts of the NH_2 precursor (NH_3 (99.98%, BOC)), the CH_3CHO co-reagent (Sigma-Aldrich, ≥99.0%), and CH_4 (99.995%, BOC). These reagent and bath gases were combined in the required quantities in a mixing manifold using calibrated mass flow controllers (MFCs; MKS Instruments). Both the bath gases and the CH_4 were introduced as pure gases, while the NH_3 was introduced as a dilute mixture of ~10% in Ar. The dilute NH_3 flow typically accounted for less than 0.2% of the total flow, resulting in ~0.02% NH_3 present in the gas expansions. The CH_3CHO co-reagent was introduced by entraining CH_3CHO vapour in a flow of the bath gas passing through a glass bubbler (a modified Dreschel bottle) containing CH_3CHO liquid. By measuring the pressure of the bath gas over the CH_3CHO, the concentration of CH_3CHO entrained in the gas flow was determined *via* its known vapour pressure,[18] and confirmed by UV absorption spectroscopy (see ESI Section S2†).

NH_2 radicals were generated from the PLP of NH_3 at 213 nm (Reaction (R2)) by the 5th harmonic of a Nd:YAG laser (Quantel Q-Smart 850), with a typical pulse energy of ~10 mJ. NH_2 radicals were observed by time-resolved LIF spectroscopy, probing the $A\ ^2A_1$ (0,9,0) ← $X\ ^2B_1$ (0,0,0) transition near 597.7 nm (ref. 19 and 20) using the output of a Nd:YAG pumped dye laser (a Quantel Q-smart 850 pumping a Sirah Cobra-Stretch). The non-resonant fluorescence at ~620 nm was collected *via* a series of lenses through an optical filter (Semrock Brightline interference filter, $\lambda_{max} = 620$ nm, fwhm = 14 nm), and observed by a temporally gated channel photomultiplier (CPM; PerkinElmer C1952P), mounted at 90° to both laser

beams. The temporal evolution of the LIF signal was recorded by varying the time delay between the photolysis and probe lasers. A typical time-resolved LIF profile (Fig. 1) consisted of 165 delay steps and resulted from the average or between 5 and 15 individual delay scans.

$$NH_3 + \hbar\nu\ (213\ nm) \rightarrow NH_2 + H \qquad (R2)$$

Photolysis of NH_3 produces both ground and vibrationally excited NH_2,[20,21] and as a consequence of this the profiles of NH_2 ($v = 0$) exhibit a growth resulting from the relaxation of vibrationally excited NH_2 (see Fig. 1). As kinetics measurements are limited by the dynamic time of the low temperature expansions, it was important that this relaxation was as efficient as possible, in order to maximise the time in which we could observe the loss of NH_2 ($v = 0$). As such, CH_4, which has been shown to efficiently relax NH_2 ($v > 0$),[9] was added to our gas flows.

Experiments looking at the dimerization of CH_3CHO at low temperatures were conducted using the same experimental apparatus as described above. CH_3CHO was observed by probing the $^3(n,\pi^*)\ A\ ^3A'' \leftarrow X\ ^1A'$ transition at 308.0 nm,[22] using the frequency doubled output of a Nd:YAG pumped dye laser (same system as described above with a BBO doubling crystal). The non-resonant fluorescence at $\lambda > 390$ nm was discriminated using a long pass Perspex filter.

Some additional experiments were also carried out observing the production of OH radicals from the reaction of CH_3CO with O_2 (R4), in order to obtain the yield of CH_3CO produced from reaction (R1) (*via* channel (R1a)). As a part of these experiments, the temporal removal of OH by CH_3CHO, both with and without O_2 present, was also recorded, with the OH produced by the PLP of *tert*-butyl

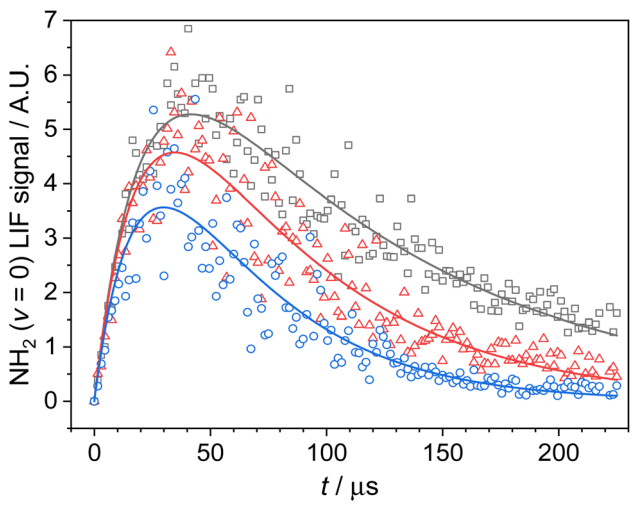

Fig. 1 NH_2 ($v = 0$) temporal traces collected at 52.2 K, a total Ar density of 6.2×10^{16} molecules per cm^3, $[NH_3] = 2.5 \times 10^{13}$ molecules per cm^3, $[CH_4] = 1.8 \times 10^{15}$ molecules per cm^3, and $[CH_3CHO]$ of 1.3, 2.8 and 5.1×10^{14} molecules per cm^3 (grey squares, red triangles, and blue circles respectively). Solid lines are the least squares fitting of a bi-exponential function to the traces from which k'_{obs} is obtained (see Section 3.1 for details).

hydrogen peroxide ($(CH_3)_3COOH$; *t*BuOOH). These experiments were all conducted using the same experimental apparatus as described above. The *t*BuOOH precursor was introduced in the same method as the CH_3CHO co-reagent, by entraining its vapour in a flow of bath gas passing through a bubbler containing *t*BuOOH liquid (Alfa-Aesar, 70% aqueous solution). The concentration of *t*BuOOH in our low temperature flows was estimated using its known vapour pressure at room temperature, and confirmed by UV absorption spectroscopy (see ESI Section S2†). OH radicals were observed by probing the $A^2\ \Sigma^+\ (v' = 0) \leftarrow X^2\ \Pi\ (v'' = 0)$ transition at ~307.9 nm, using the laser system as described above. The resonant fluorescence was collected using a gated photomultiplier tube, in which the scattered laser probe light was gated out, fitted with an interference filter centred at 308.5 nm (Barr Associates, fwhm = 5 nm).

2.2 Theoretical calculations

All *ab initio* electronic structure calculations were carried out using the Gaussian 09 programme.[23] Geometric structures of the stationary points involved (reactants, products, and intermediates including adducts, pre-reaction complexes (PRCs), and transition states (TSs)) were optimised at the M062X/aug-cc-pVTZ level of theory,[24–27] using the ultrafine integration grids in Gaussian. Rotational constants, harmonic vibrational frequencies, and zero-point energies (ZPEs) were obtained from the same level of theory. TSs were found to have only one imaginary vibrational frequency, while for the reactants, products and intermediates, all of the vibrational frequency values were positive. ZPEs obtained from the harmonic frequencies were corrected with a scaling factor of 0.956 for M062X/aug-cc-pVTZ.[28] Intrinsic reaction coordinate (IRC) calculations were performed for all the TSs identified to verify their linkage with the respective local minima on the PES. More accurate single-point energy values were obtained at the CCSD(T)/aug-cc-pVTZ level[29,30] upon the optimised structures. RRKM calculations were performed using the Master Equation Solver for the Multi-Energy Well Reactions (MESMER) program.[31]

3. Results

3.1 Kinetics

Typical NH_2 ($v = 0$) LIF temporal profiles produced following the PLP of NH_3 can be seen in Fig. 1. As can be seen from these profiles there is an initial growth in the NH_2 signal, with no instant signal observed. As discussed above, this growth in the NH_2 ($v = 0$) signal is due to relaxation of vibrationally excited NH_2 produced following the photolysis of NH_3. Although the growth of the NH_2 ($v = 0$) signal is not strictly a single exponential growth (due to the presence of several vibrationally excited states relaxing down), we were able to fit the NH_2 traces satisfactorily treating the growth as a single process:

$$NH_2\ (v \geq 1) + X \xrightarrow{k_{rel}} NH_2\ (v = 0) + X \qquad (R3)$$

where X can be CH_4, the bath gas, NH_3, and the co-reagent R under investigation. In practice, relaxation by the bath gas (Ar, He, or N_2) is slow,[32,33] necessitating the addition of CH_4 to our flows to promote efficient vibrational relaxation. Together with the reaction for the removal of NH_2 ($v = 0$):

$$NH_2\ (v=0) + CH_3CHO \xrightarrow{k_1} \text{products} \quad \text{(R1)}$$

and as experiments were carried out under pseudo-first-order conditions (*i.e.* $[NH_2] \ll [CH_3CHO]$ and $[CH_4]$), the temporal evolution of the NH_2 ($v = 0$) LIF signal (which is proportional to the NH_2 ($v = 0$) concentration) is given by:

$$[NH_2\ (v=0)]_t = \left(\frac{k'_{rel}}{k'_{obs} - k'_{rel}}\right)[NH_2\ (v \geq 1)]_0 \left(\exp^{-k'_{rel}t} - \exp^{-k'_{obs}t}\right) \quad \text{(E1)}$$

and

$$k'_{obs} = k_1[R] + k'_{loss} \quad \text{(E2)}$$

where k'_{rel} and k'_{obs} are the pseudo-first-order rate coefficients for the reactions producing and removing NH_2 ($v = 0$), $[NH_2\ (v \geq 1)]_0$ is the initial amount of NH_2 ($v \geq 1$) produced following photolysis of NH_3 that is subsequently relaxed down to NH_2 ($v = 0$), and k'_{loss} is the total rate coefficient for other loss processes of NH_2 ($v = 0$), such as diffusion out of the probe laser beam volume. Eqn (E1) was fitted to the NH_2 ($v = 0$) temporal profiles, and the parameters k'_{rel}, k'_{obs}, and $[NH_2\ (v \geq 1)]_0$ extracted. As can be seen from Fig. 1, the NH_2 traces are satisfactorily fit using a biexponential function, indicating the validity of treating the growth of the NH_2 ($v = 0$) signal as a single process. Plotting k'_{obs} *vs.* $[CH_3CHO]$ should then yield a straight line (eqn (E2)), with a gradient equal to the bimolecular rate constant, k_1, and intercept k'_{loss}. An example of such a bimolecular plot can be seen in Fig. 2. As can be seen from Fig. 2, in some of our bimolecular plots we observe a curvature in the k'_{obs} values at high $[CH_3CHO]$, which we attribute to the formation of CH_3CHO dimers in our low temperature flows. Depending on the reactivity of the dimer with NH_2 compared to the monomer, the bimolecular plots may curve

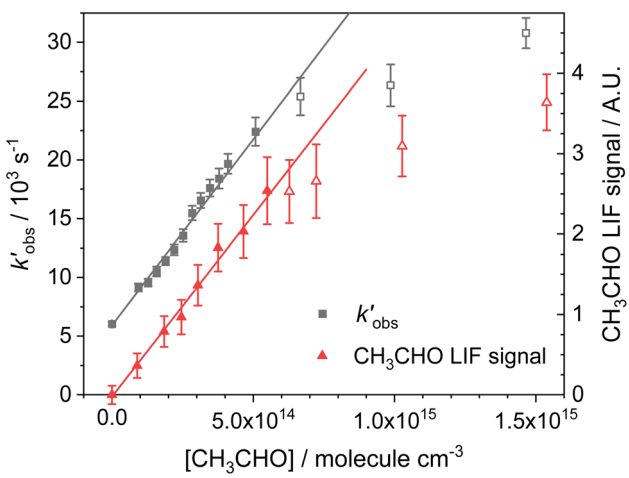

Fig. 2 Left axis: bimolecular plot of k'_{obs} *vs.* $[CH_3CHO]$ for the reaction between NH_2 + CH_3CHO (R1). Right axis: dimerization experiments observing CH_3CHO LIF signal *vs.* $[CH_3CHO]$. The deviation from linearity above approximately 5.5 $\times 10^{14}$ molecules per cm^3 CH_3CHO in both plots indicates significant dimer formation above this concentration. All data collected at 52.2 K and a total Ar density of 6.2 $\times$ 10^{16} molecules per cm^3.

upwards or downwards, or display no curvature if the dimer removes NH_2 at exactly twice the rate as the monomer. In order to help identify at which CH_3CHO concentration significant amounts of dimers form, experiments were carried out monitoring the relative concentration of CH_3CHO in the flow *via* laser-induced fluorescence as a function of the [CH_3CHO] added (see Fig. 2). In regions in which little or no dimerization is occurring, the amount of CH_3CHO monomer present in the flow will increase linearly with the [CH_3CHO] added; as such the CH_3CHO LIF signal will increase linearly (closed red triangles in Fig. 2). However, in regions in which CH_3CHO dimerization is occurring, the amount of CH_3CHO monomer present in the flows will actually be less than the [CH_3CHO] added, and as such the CH_3CHO LIF signal will begin to curve over with increasing [CH_3CHO] (open red triangles in Fig. 2). These dimerization experiments were carried out for each low temperature uniform flow employed in this study. When determining the bimolecular rate coefficient, k_1, from a bimolecular plot, only data in the linear region below the CH_3CHO concentration at which dimers formed were used (solid black squares in Fig. 2). As can be seen from Fig. 2, both the bimolecular plot and the dimerization plot exhibit the same shape with increasing [CH_3CHO] and are in good agreement on the concentration at which CH_3CHO dimers begin to form (above 6×10^{14} molecules per cm^3).

The bimolecular rate coefficients for the reaction of NH_2 with CH_3CHO (R1) determined in this study are presented in Table 1. The errors reported are the 1σ confidence intervals of the linear least squares fits of the bimolecular plots. A selection of these results recorded using He as a bath gas are shown in Fig. 3. Presenting only those rate coefficients collected in a particular bath gas and at the same approximate pressure, it can be seen that the reaction exhibits a clear negative temperature dependence over the temperature range investigated (see Fig. 3 top panel and Fig. S3†). By presenting the rate coefficients collected at the same approximate temperature (from the same nozzle) and again in the same bath gas, it can also be seen that the reaction exhibits a strong positive pressure dependence over the pressure range investigated (see Fig. 3 bottom panel and Fig. S4†). Both the negative T dependence and the positive P dependence are indicative of reactions with a pre-reaction complex on their potential energy surface (PES; see Fig. 7). There have been no previous studies of the reaction between NH_2 and CH_3CHO at low temperatures, and only one study at higher temperatures, over the temperature range 297–543 K, conducted using an isothermal discharge flow system.[34] These high temperature rate coefficients are compared with our theoretically determined rate coefficients in Section 4, and in Fig. S13.†

3.2 NH_2 ($v > 0$) removal

The strong pressure dependence of reaction (R1), which at certain temperatures and with certain bath gases exhibited an almost 1 : 1 relationship between rate coefficient and pressure, was slightly unexpected, and indicated that the reaction is firmly within the low-pressure region over the pressures investigated (1.4–28.2 $\times 10^{16}$ molecules per cm^3). In contrast, the reaction between OH and CH_3CHO, which has also been studied at low temperatures, does not exhibit any pressure dependence over the temperature and pressure range of 21–106 K and 1–20 $\times 10^{16}$ molecules per cm^3, respectively.[35] One method for estimating the high-

Table 1 Bimolecular rate coefficients for the reaction between NH_2 + CH_3CHO together with relevant experimental conditions

Nozzle	Gas	$\sim T^a$/K	T^b/K	Density^b/10^{16} molecules per cm^3	$k_1{}^c$/10^{-11} cm^3 per molecule per s
1	Ar	31	34.2 ± 3.0	2.1 ± 0.3	3.77 ± 0.61
			30.3 ± 2.7	3.4 ± 0.4	5.82 ± 0.45
			28.7 ± 2.6	6.2 ± 0.8	10.7 ± 1.9
	He	37	42.2 ± 5.4	2.6 ± 0.5	1.74 ± 0.50
			37.2 ± 3.1	4.6 ± 0.6	3.56 ± 0.54
			35.0 ± 2.8	6.1 ± 0.7	3.69 ± 0.53
			34.3 ± 3.4	8.8 ± 1.3	4.72 ± 0.91
	N_2	66	70.0 ± 2.7	1.4 ± 0.1	0.25 ± 0.27
			67.1 ± 2.1	2.5 ± 0.2	0.84 ± 0.38
			67.1 ± 2.1	2.5 ± 0.2	1.53 ± 0.33
			64.6 ± 2.0	4.5 ± 0.3	0.92 ± 0.39
			62.9 ± 2.4	6.4 ± 0.6	2.80 ± 0.31
2	Ar	45	52.2 ± 2.9	6.2 ± 0.5	3.17 ± 0.09
			47.0 ± 2.8	11.2 ± 1.0	4.37 ± 0.41
			41.6 ± 1.6	28.2 ± 1.6	9.88 ± 0.90
			39.3 ± 2.7	16.5 ± 1.7	8.46 ± 0.37
	He	51	55.4 ± 3.8	10.0 ± 1.0	1.76 ± 0.10
			55.4 ± 3.8	10.0 ± 1.0	1.56 ± 0.09
			50.9 ± 1.9	17.9 ± 1.0	3.48 ± 0.25
			47.6 ± 1.5	23.5 ± 1.2	3.89 ± 0.38
	N_2	83	89.9 ± 2.5	4.2 ± 0.3	0.72 ± 0.10
			84.4 ± 2.8	7.4 ± 0.6	0.57 ± 0.22
			80.5 ± 2.9	13.0 ± 1.2	2.57 ± 0.31
			78.4 ± 2.9	17.7 ± 1.6	1.43 ± 0.42
3	Ar	45	47.9 ± 4.3	6.2 ± 0.8	4.89 ± 0.11
			44.4 ± 4.3	11.2 ± 1.6	9.95 ± 0.91
			43.3 ± 4.3	15.9 ± 2.3	11.6 ± 0.7
	He	52	54.6 ± 4.0	7.4 ± 0.8	1.4 ± 0.12
			51.8 ± 3.7	10.1 ± 1.1	2.3 ± 0.12
			49.6 ± 3.9	14 ± 1.6	3.13 ± 0.18
	N_2	89	92.9 ± 6.6	5.3 ± 0.9	0.17 ± 0.05
			87.4 ± 6.4	9.1 ± 1.7	0.92 ± 0.18
			85.6 ± 6.0	12.7 ± 2.2	1.14 ± 0.18
4	Ar	55	59.4 ± 7.4	8.8 ± 1.6	3.7 ± 0.21
			54.2 ± 7.9	15.0 ± 3.2	6.28 ± 0.59
			52.4 ± 7.8	20.5 ± 4.5	9.69 ± 0.61
	He	62	63.2 ± 6.2	6.8 ± 0.9	0.80 ± 0.14
			62.9 ± 5.7	13.5 ± 1.9	0.73 ± 0.14
			60.0 ± 6.2	18.6 ± 2.9	1.61 ± 0.22
	N_2	101	106.7 ± 8.6	7.6 ± 7.6	0.42 ± 0.04
			99.5 ± 9.8	12.7 ± 3.1	0.21 ± 0.03
			97.0 ± 9.7	17.7 ± 4.3	0.21 ± 0.08

[a] Average T of the low temperature flows for a particular nozzle and a particular gas. [b] Uncertainties in each value of T and density are $\pm 1\sigma$ (the standard deviation) of the measured T and density along the axis of the Laval expansion. [c] Uncertainties reported at the 1σ level for the linear least-squares fitting of the pseudo-first-order coefficients as a function of [CH_3CHO].

pressure limit of a reaction is the proxy method,[36,37] in which the loss of vibrationally excited NH_2 with CH_3CHO is measured. Here, the assumption is made that following the formation of the collision complex, the excess vibrational

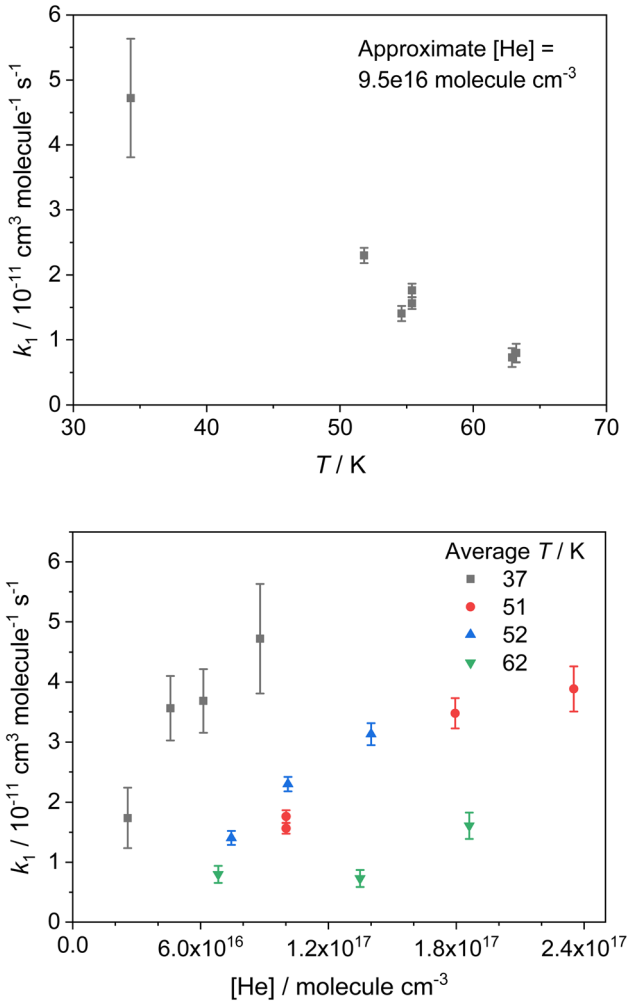

Fig. 3 Selected T and P dependent rate coefficients, collected in He bath gas, for the reaction NH_2 + CH_3CHO (R1). Top panel: T dependent rate coefficients collected at an approximate He density of 9.5×10^{16} molecules per cm^3; bottom panel: P dependent rate coefficients collected at approximate temperatures of 37 K (grey squares), 51 K (red circles), 52 K (blue upward triangles), and 62 K (green downward triangles). Each T corresponds to a different Laval nozzle (1–4 respectively).

energy in the NH_2 is rapidly redistributed among the many other modes in the complex, and any NH_2 formed following dissociation of the complex is in $v = 0$. Thus, the proxy method provides an estimate of the capture rate coefficient for complex formation, which can be used as the inverse Laplace transform (ILT) parameters for the initial association reaction of NH_2 with CH_3CHO in our MESMER calculations (Section 4).

Rate coefficients for the removal of NH_2 ($v = 0$, x, 0) with CH_3CHO, where $x =$ 0–4 and represents vibrational excitement of the ν_2 bending mode in NH_2, are presented in Fig. 4 and Table 2, together with the transitions and wavelengths

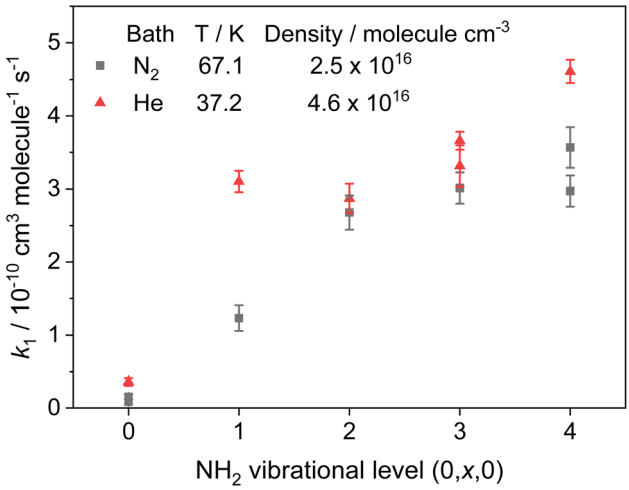

Fig. 4 Rate coefficients for the removal of NH_2 ($v = 0$–4) with CH_3CHO. Grey squares; $T =$ 67.1 K, $[N_2] = 2.5 \times 10^{16}$ molecules per cm^3. Red triangles; $T = 37.2$ K, [He] $= 4.6 \times 10^{16}$ molecules per cm^3.

Table 2 Rate coefficients for the removal of NH_2 ($v_2 = 0$–4) by CH_3CHO

			$k^b/\times10^{-10}$ cm^3 per molecule per s	
v_2	Transition[a]	λ/nm	In N_2 at 67.1[c] K	In He at 37.2[d] K
0	0,9,0 ← 0,0,0	597.7	0.08 ± 0.04	0.54 ± 0.05
			0.15 ± 0.03	—
1	0,11,0 ← 0,1,0	591.1	1.23 ± 0.18	3.1 ± 0.15
2	0,12,0 ← 0,2,0	607.2	2.68 ± 0.23	—
		608.4	—	2.87 ± 0.2
3	0,13,0 ← 0,3,0	628.9	3.01 ± 0.21	3.31 ± 0.28
		627.4	—	3.66 ± 0.12
4	0,16,0 ← 0,4,0	611.0	3.57 ± 0.28	4.61 ± 0.16
		616.8	2.97 ± 0.21	—

[a] $A\ ^2A_1 \leftarrow X\ ^2B_1$ transition. [b] Uncertainties reported at the 1σ level for the linear least-squares fitting of the pseudo-first-order coefficients as a function of $[CH_3CHO]$. [c] Collected using nozzle 1 at $T = 67.1$ K and $[N_2] = 2.5 \times 10^{16}$ molecules per cm^3. [d] Collected using nozzle 1 at $T = 37.2$ K and [He] $= 4.6 \times 10^{16}$ molecules per cm^3.

employed.[21,38] In experiments monitoring removal of NH_2 ($v = 1$–4), no CH_4 was added to the low temperature flows, and a Perspex filter was used to collect the fluorescence and cut out the scattered laser light from the 213 nm photolysis pulse. As can be seen from Fig. 4 and Table 2, removal of vibrationally excited NH_2 by CH_3CHO is significantly faster than removal of ground state NH_2, with higher vibrational levels appearing to be removed faster than lower vibrational levels. However, the rate coefficient does appear to be reaching a limit (the high-pressure limit) at high v; at 37.2 K in He this limit is practically reached by $v = 1$, and appears around 4×10^{-10} cm^3 per molecule per s (assessed visually), while at 67.1 K in N_2 the limit is not reached until around $v = 2$ or 3, and appears to be around

3.5×10^{-10} cm^3 per molecule per s. These results suggest that for the NH_2 + CH_3CHO system, only at the lowest temperatures are the initial collision complexes long-lived enough to ensure complete redistribution of the excess vibrational energy from the NH_2 species into the complex, and that at higher temperatures some complexes may dissociate before this has happened. Thus, proxy method estimations of the high-pressure limit for other systems carried out looking at the removal of $v = 1$ only, may underestimate the true limit. However, as the results at 67.1 K in N_2 show, the redistribution of energy from higher vibrational states appears to be faster, suggesting the high-pressure limit may still be estimated by looking at removal from successively higher vibrational levels. The slightly larger high-pressure limit at 37.2 K suggests a small negative temperature dependence in the initial association reaction between NH_2 and CH_3CHO.

3.3 OH/CH_3CO yields

OH LIF profiles produced following the photolysis of NH_3 in the presence of both CH_3CHO and O_2 are presented in Fig. 5. The OH observed is the result of CH_3CO, the product of reaction (R1a), reacting with O_2 to produce OH (R4):

$$CH_3CO + O_2 \rightarrow OH + \text{co-products} \quad (R4)$$

As the experiments were carried out under pseudo-first-order conditions (*i.e.* $[NH_2] \ll [CH_4]$, $[CH_3CHO]$, and $[O_2]$), the growth and loss of the OH signal can be described by a bi-exponential function of the form:

$$[OH]_t = f_{OH}\left(\frac{k'_{growth}}{k'_{loss} - k'_{growth}}\right)[NH_2]_0\left(\exp^{-k'_{growth}t} - \exp^{-k'_{loss}t}\right) \quad (E3)$$

where k'_{growth} and k'_{loss} are the pseudo-first-order rate coefficients for the reactions producing and removing OH, $[NH_2]_0$ is the initial amount of NH_2 produced following PLP of NH_3, and f_{OH} is the observed OH fluorescence signal, or OH yield (note, the reaction of $CH_3CO + O_2$ can also lead to other products). As OH itself reacts with CH_3CHO (R5), its primary loss is the sum of (R5) and diffusional losses. Although the OH profiles are not strictly bi-exponential in nature, as the growth of the OH signal is the result of series of subsequent reactions (vibrational relaxation of NH_2^* by CH_4 (R3), reaction of NH_2 with CH_3CHO to form CH_3CO (R1a), and reaction of CH_3CO with O_2 to form OH (R4)), they could be satisfactorily fit using eqn (E3), and the parameters k'_{growth}, k'_{loss}, and f_{OH} extracted.

The OH yields themselves do not give the yield for CH_3CO production from reaction (R1). To do this requires two additional pieces of knowledge; the first is an understanding of how many OH radicals have been produced relative to the initial number of NH_2 radicals produced, while the second is an understanding of the yield of OH from the reaction of CH_3CO with O_2 (ϕ_{OH}; R4). The second can be determined by measuring the rate coefficient for the removal of OH by CH_3CHO (R5) both with and without O_2 present.[39,40] In the experiments with O_2 present, CH_3CO formed by reaction (R5) will react with O_2, with a fraction regenerating OH (R4). If the concentration of O_2 is great enough such that the reaction between CH_3CO and O_2 is fast compared to the OH + CH_3CHO reaction (*i.e.* $k'_4 \gg k'_5$), then

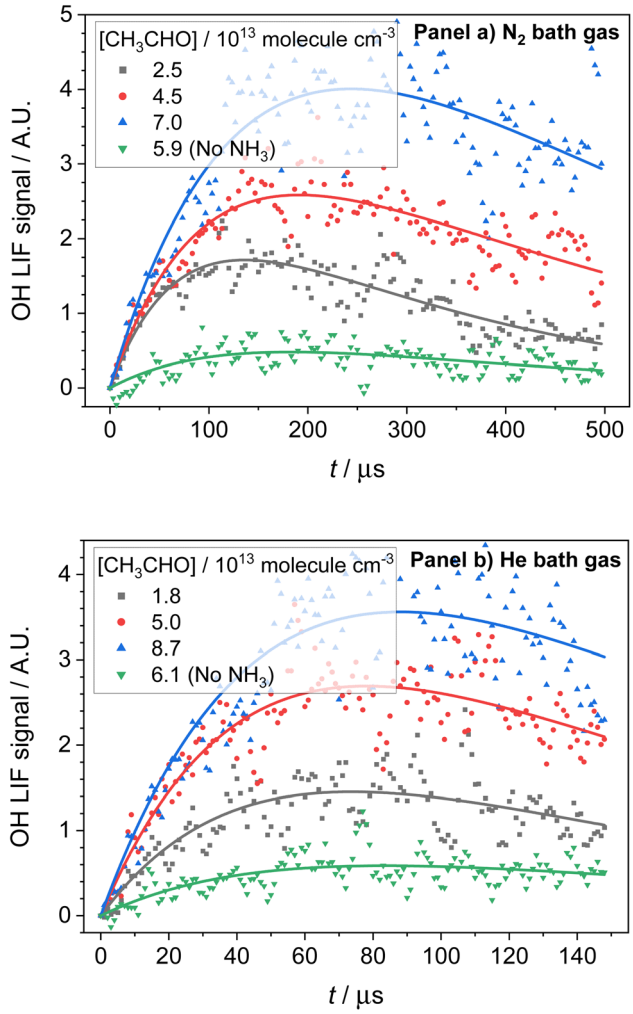

Fig. 5 OH traces collected following photolysis of NH_3 in the presence of varying amounts of CH_3CHO and O_2. Panel (a) traces collected at 67.1 K, a total N_2 density of 2.5×10^{16} molecules per cm^3, $[NH_3] = 1.4 \times 10^{13}$ molecules per cm^3, $[CH_4] = 8.3 \times 10^{14}$ molecules per cm^3, and $[O_2] = 8.2 \times 10^{14}$ molecules per cm^3. Panel (b) traces collected at 35.0 K, a total He density of 6.1×10^{16} molecules per cm^3, $[NH_3] = 1.2 \times 10^{13}$ molecules per cm^3, $[CH_4] = 8.4 \times 10^{14}$ molecules per cm^3, and $[O_2] = 8.3 \times 10^{14}$ molecules per cm^3. The green downward triangles in both plots are collected with no NH_3 present, indicating a small contribution of OH from the photolysis of CH_3CHO in the presence of O_2.

the OH removal will be determined by the fraction of (R5) that does not regenerate OH. As such, the reduction in the bimolecular rate coefficient for OH loss with CH_3CHO in the presence of O_2, k_{O_2}, as compared to without O_2, $k_{\text{no } O_2}$, gives the OH yield:

$$\phi_{OH} = 1 - k_{O_2} \Big/ k_{\text{no } O_2} \quad \text{(E4)}$$

$$OH + CH_3CHO \rightarrow CH_3CO, + \text{other products} \quad (R5)$$

Experiments monitoring the loss of OH by CH_3CHO, both with and without O_2 present, were carried out at $T = 67.1$ K in N_2 bath gas. OH LIF traces collected in these experiments (see Fig. S5†) could be fit with a single exponential loss in order to obtain the observed pseudo-first-order loss rate, k'_{obs}. Bimolecular plots obtained by plotting k'_{obs} *vs.* $[CH_3CHO]$ can be seen in Fig. 6, in which the clear reduction in the bimolecular rate coefficient with O_2 can be seen. With no O_2 present, we obtain a value of $k_{5(no\ O_2)} = (9.81 \pm 0.57) \times 10^{-11}$ cm^3 per molecule per s. This rate coefficient is in good agreement with a recent literature study of the low temperature reaction of OH with C_3HCHO, in which they obtain a rate coefficient of $(1.25 \pm 0.13) \times 10^{-10}$ cm^3 per molecule per s at $T = 64$ K.[35] With O_2 present, we obtain a value of $k_{5(O_2)} = (5.4 \pm 4.2) \times 10^{-12}$ cm^3 per molecule per s, giving a value of $\phi_{OH} = 0.94 \pm 0.05$.

To address the first issue in determining the yield for CH_3CO production from (R1), that is understanding how many OH radicals have been produced relative to the initial number of NH_2 radicals produced, we used the following procedure. In these experiments, we are photolyzing a known amount of NH_3 to produce NH_2 radicals, which go on to form a number of OH radicals which we observe using LIF. Using both the concentration and absorption cross section of NH_3 we are able to estimate the number of NH_2 radicals produced in our system. This calculation also requires the energy of the photolysis laser, however as this is kept constant in our experiments, this will later cancel out in our calculations and can be ignored. To put the OH signal we observe on an absolute scale, we then calibrate our OH LIF signal in a separate experiment by photolyzing a known amount of *t*BuOOH under the same conditions and using the same photomultiplier settings. Again, as we know both the concentration and absorption cross section of *t*BuOOH, we

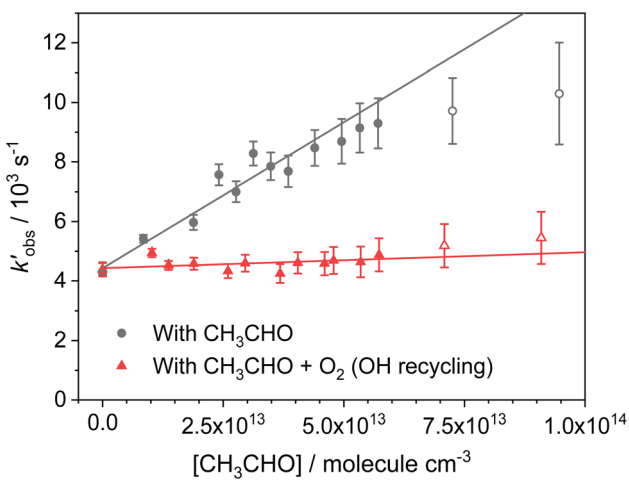

Fig. 6 Bimolecular plot of k'_{obs} *vs.* $[CH_3CHO]$ for the reaction between OH + CH_3CHO (R5). Grey circles; OH loss with only CH_3CHO present. Red triangles; OH loss with both CH_3CHO and O_2 present. Curvature of the grey circles at $[CH_3CHO]$ above 7×10^{13} molecules per cm^3 indicates significant dimer formation, with the linear fits obtained only using data points below this.

can determine the number of OH radicals present in our system giving us our OH LIF signal. In this manner we can determine a ratio of how many OH radicals we observe compared to the initial number of NH_2 radicals produced. In these calculations we account for the reduction in the initial NH_3 concentration in our system due to removal by CH_3CHO, and for the non-unity conversion of CH_3CO to OH by O_2. Using this method, we have determined CH_3CHO yields from reaction (R1) (*i.e.* the branching ratio for reaction (R1a)) to be 0.029 ± 0.014 at $T = 67.1$ K and $[N_2] = 2.50 \times 10^{16}$ molecules per cm^3, and 0.026 ± 0.008 at $T = 35.0$ K and $[He] = 6.14 \times 10^{16}$ molecules per cm^3. A more detailed account of how we determined these CH_3CO yields is given in the ESI in Section S6.†

4. Discussion

4.1 *Ab initio* calculations of the PES

A schematic of the full PES for the reaction between NH_2 and CH_3CHO can be seen in Fig. 7. The energies given are at the CCSD(T) level of theory and include ZPEs calculated at the M062x level. The optimised structures of the stationary points are given in Fig. S7 in the ESI,† together with the full molecular properties in Tables S8–S10.† As can be seen from Fig. 7, the reaction initially proceeds *via* the formation of one of two pre-reaction complexes (PRCs; labelled PRC1 and PRC2 in Fig. 7). PRC1, in which the NH_2 moiety is located over the acetyl H/C=O end of the acetaldehyde, is linked to the formation of the acetyl H-abstraction products NH_3 + CH_3CO *via* TS1 (+17.3 kJ mol^{-1}). PRC2, in which the NH_2 moiety is located above the methyl/C=O end of the acetaldehyde, is linked to two product channels; the methyl H-abstraction channel products NH_3 + CH_2CHO *via*

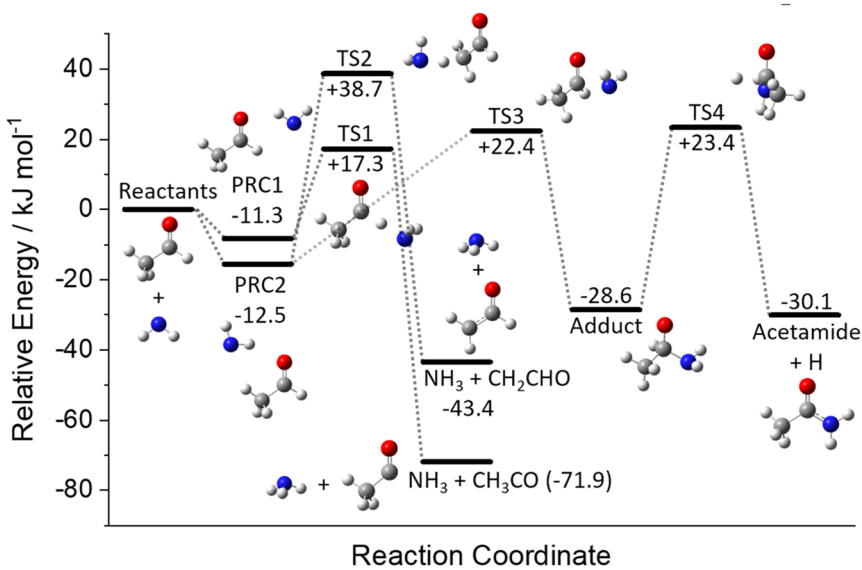

Fig. 7 Potential energy surface for NH_2 + CH_3CHO determined at the CCSD(T)/aug-cc-pVTZ//M062X/aug-cc-pVTZ level of theory. All energies are in kJ mol^{-1} and are corrected with scaled zero-point vibrational energy.

TS2 (+38.7 kJ mol^{-1}), and the addition–elimination channel products acetamide + H. The acetamide + H product channel requires the initial formation of a bound adduct from PRC2 *via* TS3 (+22.4 kJ mol^{-1}), followed by the elimination of an H atom to form products *via* TS4 (+23.4 kJ mol^{-1}). As both the H-abstraction channels involve the transfer of an H-atom, quantum mechanical tunnelling is likely to play a role at low temperatures.

There have been no previous theoretical investigations into the reaction between NH_2 and CH_3CHO; however, the reaction between NH_2 and formaldehyde (CH_2O) has been studied.[9,41–44] As expected, considering the similarity between the two systems, the PESs for the two reactions resemble each other remarkably well, in both the depth of the PRCs (where mentioned) and the heights of the barriers; the only significant difference is the additional methyl-H abstraction channel present in the case of NH_2 + CH_3CHO.

4.2 Rate theory calculations using MESMER

Using the calculated NH_2 + CH_3CHO PES surface given in Fig. 7, rate coefficients and branching ratios for the reaction over a wide range of temperatures and pressures have been calculated using the MESMER program.[31] The inverse Laplace transform (ILT) parameters for the association reaction of NH_2 with acetaldehyde, which take the form of a modified Arrhenius function $A(T/300)^n$ (with the activation energy being set to zero), were adjusted to give good agreement to the high pressure limits determined in Section 3.1, with the values $A = 2.5 \times 10^{-10}$ cm^3 per molecule per s and $n = -0.25$ used. Initial calculations carried out using the full PES have shown that the acetamide + H product channel (R1c) is predicted to be a very minor channel at all temperatures and pressures (over the range 20–400 K and 1×10^{11} to 1×10^{24} molecules per cm^3). Indeed, at a pressure of [Ar] = 1×10^{16} molecules per cm^3, the channel (R1c) only accounts for 0.1% of the product yield at 400 K, and decreases with decreasing temperature, becoming insignificant below ~150 K (see ESI Fig. S11†). This is due to the relatively high barrier to adduct formation (TS3, 22.4 kJ mol^{-1}) effectively turning off this channel at low temperatures as there is no coordinate for H-atom tunnelling under this barrier. As such, for the MESMER calculations discussed below, a simplified PES was used, in which the channel (R1c) was excluded (see ESI Fig. S12†).

Rate coefficients predicted by MESMER using the surface given in Fig. S12† and at a pressure of 1×10^{17} molecules per cm^3, are compared with our experimental data collected at a similar pressure in Fig. S13.† As can be seen from Fig. S13,† the experimental rate coefficients are significantly faster than those predicted by MESMER, by around 2 orders of magnitude. However, both the experimental and MESMER rate coefficients show a strong positive pressure dependence and a negative temperature dependence. This T and P dependence is the result of the formation of the weakly bound pre-reaction complexes on the PES. As the pressure is increased, there is more chance for the excess energy in the incoming reactants to be removed by collisions and for stabilization into the potential well to occur, while at the same time as the temperature is lowered, the rate of dissociation of the PRCs back to products will also decrease, increasing the effective loss rate of the reactants. Looking at species time profiles produced by MESMER, it can be seen that on the timescales of our experiments, as the

reactants are lost we see significant population of the PRCs, which eventually go on to form products on longer timescales *via* quantum mechanical tunnelling. Thus, the fast removal rates of NH_2 we observe in our experiments correspond to the population of the PRCs. How MESMER calculates the stabilization of the reactants into the PRC wells is dependent on the description of the molecular parameters of the species involved in the reaction scheme, and in particular how these affect the density of states of the reactants and adducts. The significantly smaller rate coefficients predicted by MESMER compared to experiment suggest an underestimation in the calculation of the density of states of the PRCs as compared to the reactants.

The approximation of the harmonic oscillator was used for the vibrational frequencies in the calculation of the density of states. However, a few vibrational frequencies may be better represented by the hindered rotor (HR) approximation. Typically, treating low frequency vibrations as HRs increases the density of states. Fig. S14† shows all the rotations described with the HR approach. HR potentials were constructed through an *ab initio* calculation of a relaxed scan of the energy as the dihedral angle respective to the rotation is changed, with steps of 5°. A partial structure optimization was performed at the end of every step, until a 360° coverage was obtained. Both PRCs have 3 hindered rotors; rotation of the methyl group around the C–C bond, rotation of the terminal N–H around bond 7, and rotation of the N around bond 9 (see Fig. S14† for bond labels). For the hindered rotors around bond 9, we were only able to obtain a potential around ~180° of the dihedral when carrying out a relaxed scan, due to the O–H–N angle approaching linearity and causing difficulties in the representation of the dihedral in Gaussian. However, by carrying out a fixed scan an approximation of the potential around the full 360° was obtained. Surprisingly, the treatment of the rotations around bonds 4 and 7 as HRs, rather than harmonic vibrations, results in a marginal increase in the density of states in the PRCs. However, the treatment of the rotation around bond 9 as a HR does increase the density of states, especially for PRC2. This increase in the density of states results in around a 3 fold increase in the rate coefficients predicted by MESMER (between 20 and 100 K and at $[Ar] = 1 \times 10^{17}$ molecules per cm^3), bringing them closer to the experimental values (see Fig. S13†).

In order to obtain better agreement between the experimental and calculated rate coefficients, we have used MESMER to fit the experimental data by adjusting the well depths of the PRCs. In these calculations, we include the HR potentials and use the reduced $NH_2 + CH_3CHO$ PES (excluding channel (R1c), Fig. S12†), and the errors of the experimental rate coefficients were set to 20% (or kept as the experimental error if >20%). In order to reduce the computational expense when fitting the experimental data, rather than allowing the ZPEs of each PRC well to be varied independently, we set the ZPE of PRC2 to be defined from the ZPE of PRC1 minus 1.2 kJ mol^{-1}. In this manner we keep the absolute difference in energy between the two PRCs, while allowing the ZPEs of both to move up and down in tandem during the fitting.

The best fit to the experimental rate coefficients was obtained by moving the ZPEs of the PRCs down by 9.5 kJ mol^{-1}, to −20.8 and −22.0 kJ mol^{-1} for PRCs 1 and 2, respectively. The χ^2 parameter of the fit reduces from 856 (20.4 per point) using the original ZPEs down to 177 (4.2 per point) with the new values. Table S15† compares the experimental and calculated rate coefficients determined

using these new values, and gives the % difference between the two. There is reasonable agreement between the rate coefficients, with an average difference of 20% for those using He as the bath, 30% using Ar, and 55% using N_2. The larger % difference using N_2 as a bath gas is likely the result of the larger errors in the experimental rate coefficients, which are on the lower edge of what we can reasonably measure in our experiments. This increase of 9.5 kJ mol^{-1} in the well depths of the PRCs is rather large. Typically, CCSD(T) calculations would be expected to be accurate to within 5 kJ mol^{-1}, so an adjustment of almost double this suggests either some sort of systematic error or interference in the experimental results, or some error in the description and treatment of the species in the calculation. Possible sources of error in the experimental results which have been discussed above, are in the acetaldehyde concentrations in our experiments, and in the possible formation of acetaldehyde dimers. Our acetaldehyde concentrations are confirmed using UV absorption spectroscopy, and furthermore we obtain a rate coefficient for OH + CH_3CHO in good agreement with another study.[35] Regarding dimers, as we are able to directly monitor the fluorescence from acetaldehyde we are able to determine at what [CH_3CHO] significant dimers begin to form, and ensure we only determine rate coefficients below this value where the second order plot is entirely linear. Another possible source of error is due to secondary chemistry in our experiments, such as from the removal of NH_2 with a photolysis product of CH_3CHO. However we deem this unlikely, as the cross-section for CH_3CHO at 213 nm is $\sim 5 \times 10^{-22}$ cm^{-2},[45] over 3 orders of magnitude smaller than for NH_3 at 213 nm, meaning that even at the highest CH_3CHO concentrations in our experiments we would expect a ratio of NH_2 to CH_3CHO photolysis products of 40 : 1. Possible sources of error in the MESMER calculations likely lie in the description of the HRs, in particular the HR relating to rotation around bond 9 in both PRCs. The magnitude and shape of the potential for this HR has been shown to have a strong effect on the calculated density of states of the PRCs, and as such the calculated rate coefficients are sensitive to this potential. Thus, this study highlights the importance of improved computational methods in calculating low frequency vibrational frequencies and hindered rotor potentials.

In addition to fitting the rate coefficients, we are also able to fit the experimentally determined yields for CH_3CO. As discussed above, at the temperatures and pressures in our experimental setup, the loss of NH_2 that we observe in our experiments is primarily due to the formation of the PRCs (and in particular PRC2), which on timescales significantly longer than our experiments will go on to form products (both channels (R1a) and (R1b)). However, as observed in our experiments, some CH_3CO is formed on the same timescale as NH_2 is lost, which for convenience we will call instant CH_3CO. This instant CH_3CO can be thought of as the CH_3CO produced from well-skipping, and is sensitive to the height of the acetyl H-abstraction transition state (TS1). Thus, we are able to fit the height of TS1 to the experimentally determined CH_3CO yields. This is crucially important for understanding the astrochemical implications of this reaction, as the height of TS1 greatly affects the low-pressure limiting rate coefficient, which is the relevant value for interstellar environments where there is no collisional stabilisation of the pre-reactive complex. As in the case of fitting the ZPEs of the PRCs, we have kept the absolute difference in the ZPEs of the TSs for the two H-abstraction channels constant, by defining the ZPE of TS2 from the ZPE of TS1

plus 21.4 kJ mol^{-1}, while allowing the ZPEs of both to move up and down in tandem during the fitting. When entering the CH_3CO yields to be fit into MESMER, the timescale for the yield must also be entered to ensure we are fitting to the instant CH_3CO, rather than the final CH_3CO yield. This timescale must be also be consistent with the excess reagent concentration entered in the model.

Table S16† compares the calculated instant CH_3CO yields to the experimental values following fitting of the ZPEs of the H-abstraction TSs (TS1 and TS2) to the experimental data. The best fit to the experimental yields is obtained by moving the ZPEs of the H-abstraction TSs down by 0.9 kJ mol^{-1}, to 16.4 and 37.8 kJ mol^{-1} for TSs 1 and 2, respectively. This small change in the heights of the H-abstraction TSs is well within the expected error of the calculated CCSD(T) energies.

Using the ZPEs of the PRCs and TSs obtained by fitting to the experimental data, we have calculated rate coefficients and branching ratios over a wide range of temperatures and pressures. Fig. 8 gives the low-pressure limiting rate coefficients which are applicable to the interstellar medium, while the rate coefficients over the full T and P range, which may be applicable to other high-pressure environments, can be seen in Fig. S17 in the ESI.† At the low-pressure limit, the only product channel open is the $CH_3CO + NH_3$ channel (R1a). Looking at Fig. 8, a turn around in the rate can be seen at around 200 K; above this temperature we see a small positive temperature dependence, whereas below this temperature we see a strong negative temperature dependence. This sharp increase in the rate coefficient at low temperatures is the result of the PRC wells on the PES, which are sufficiently long-lived at low temperatures to allow the H-atom to quantum-mechanically tunnel through the aldehydic H-abstraction barrier (TS1) to products. This mechanism has been reported previously for a range of low temperature H-abstraction reactions involving OH and oxygenated volatile organic compounds,[11–13,35] and for $NH_2 + CH_2O$.[9] Although the product channel (R1b), producing $CH_2CHO + NH_3$, also involves the transfer of an H atom

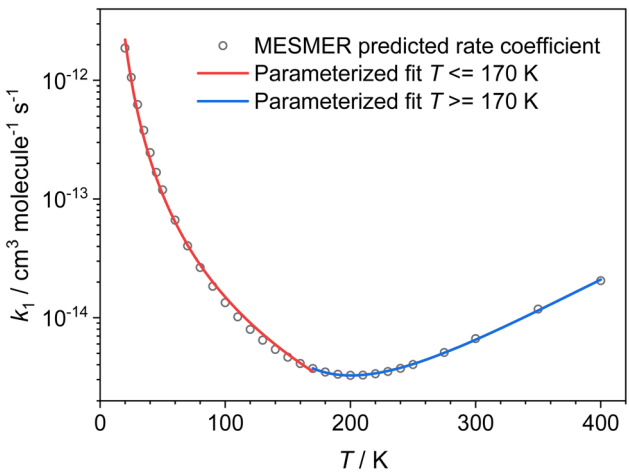

Fig. 8 Low-pressure limiting rate coefficients for the reaction between $NH_2 + CH_3CHO \rightarrow NH_3 + CH_3CO$ (R1a) calculated by MESMER, using the PRC and TS energies determined by fitting to the experimental data (see text for details).

and can occur by quantum mechanical tunnelling, due to the significantly larger barrier to methyl H-abstraction (TS2, 21.4 kJ mol^{-1} higher than TS1), and a similar imaginary frequency, the tunnelling rate through TS2 is insignificant when compared to the tunnelling rate through TS1. As such, the only products at the low-pressure limit are CH_3CO + NH_3 (R1a). The unique shape of the low-pressure limiting rate coefficient for (R1) does not allow for the parameterization of the data over the whole temperature range using a single modified Arrhenius equation. Instead, the data above and below 170 K were parameterized, giving (see red and blue solid lines in Fig. 8: units are cm^3 per molecule per s; errors are the 1σ level of a least squares fit to the data):

$$k_{(NH_2+CH_3CH\tilde{O}NH_3+CH_3CO)}\,(20 \leq T/K \leq 170) = (7.23 \pm 0.64) \times 10^{-16} \times (T/300)^{(-2.56\pm0.15)} \times \exp^{[(22.0\pm7.8)/T]}$$

$$k_{(NH_2+CH_3CH\tilde{O}NH_3+CH_3CO)}\,(170 \leq T/K \leq 400) = (9.99 \pm 1.49) \times 10^{-18} \times (T/300)^{(9.70\pm0.17)} \times \exp^{[(1944\pm44)/T]}$$

These new rate coefficients will be submitted to the Kinetic Database for Astrochemistry (KIDA),[46] and the UMIST Database for Astrochemistry (UdFA).[47]

4.3 Astrochemical implications

To assess the astrophysical implications of the measured rate constant, we ran a single-point dark cloud astrochemical model with a temperature of 10 K, a gas number density of 10^4 cm^{-3}, and a cosmic-ray ionisation rate of 1.3×10^{-17} s^{-1}. We assume that the cloud has a high visual extinction and is fully shielded from any external sources of UV radiation. We ran four variants of the model with different assumptions for the chemistry: (i) a gas-phase only model using the network from Walsh *et al.*[48] with updates as described in Douglas *et al.*,[15] (ii) a gas–grain model with the same chemistry, (iii) a gas-phase only model including the new reaction and rate constant measured in this work, and (iv) a gas–grain model including the same update. We find that the abundance of the reactants, NH_2 and CH_3CHO, and that of one of the products, NH_3, are not significantly affected when the new reaction is included in the network. However, we do see a non-negligible effect on the gas-phase abundance of the radical, CH_3CO, as shown in Fig. 9. In scenario (i), there are no efficient gas-phase routes to form this radical in the Walsh *et al.*[48] network and its abundance is effectively zero. When gas–grain chemistry is included (scenario (ii); red solid line in Fig. 9), the abundance increases to $\sim10^{-26}$ to 10^{-24} with respect to H nuclei density; however, this range is still considered negligible. In this gas–grain model, the only source of gas-phase CH_3CO is *via* cosmic-ray-induced photodesorption from the ice phase. Radicals such as CH_3CO are efficiently hydrogenated in the ice even at 10 K, and so have a very short life-time on the surface and hence reach a negligible gas-phase abundance only. When the new reaction studied here is included in the gas-phase only model (scenario (iii); blue dotted line in Fig. 9), the abundance of CH_3CO increases from $\sim10^{-20}$ to 10^{-18} with production driven solely by the included reaction. Finally, when gas–grain chemistry is included together with the new reaction studied here (scenario (iv); blue solid line in Fig. 9), the abundance of CH_3CO increases further, to the arguably non-negligible range of 10^{-14} to 10^{-12} with respect to H nuclei density beyond a time of 10^6 years. This is driven

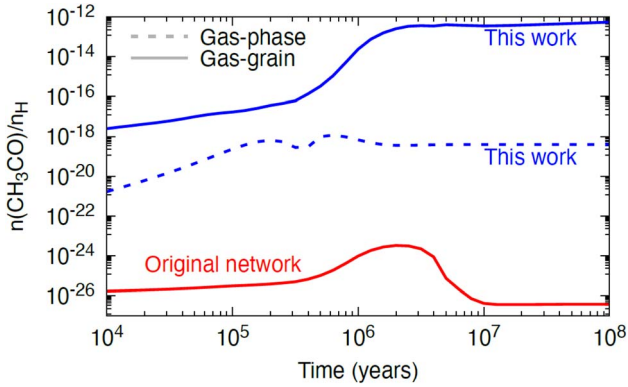

Fig. 9 The abundance of gas-phase CH_3CO with respect to hydrogen nuclei density as a function of time, a dark cloud model using three different variants of the chemical network from Walsh *et al.*[48] with: one using the gas–grain network from Walsh *et al.*[48] with the rate constants from Douglas *et al.*[15] (red solid line), one using a gas-phase only network including the gas-phase reaction studied in this work (NH_2 + CH_3CHO; dotted blue line), and one using a gas–grain network including the reaction studied in this work (solid blue line).

by the more efficient production of gas-phase CH_3CHO in the gas–grain model, for which the abundance is boosted by two orders of magnitude when grain-surface processes are included. The steady-state fractional abundance reached for gas-phase CH_3CO ($\sim 10^{-12}$) is approaching the threshold at which molecules become potentially observable in interstellar environments. For example, the methoxy radical, CH_3O, has been observed towards several dense cores, with an estimated fractional abundance of $\sim 10^{-12}$ to 10^{-11} with respect to H nuclei density.[49–51]

The model results for a dark cloud shown here, suggest that, whilst the NH_2 + CH_3CHO reaction is not a dominant loss mechanism for either reactant, nor a dominant production mechanism for NH_3, it is a potential production route for the gas-phase radical, CH_3CO, at least under dark cloud conditions. We leave exploration of the impact of this reaction on the chemistry in other astrophysical environments to future work. The gas-phase chemistry of organic radicals, such as CH_3CO, remains poorly constrained. A search of KIDA,[46] suggested only two gas-phase reactions forming this radical under astrophysical conditions (C_2H_3 + O and OH + H_2C_3O),[52,53] and no gas-phase destruction reactions.

5. Conclusions

The reaction between NH_2 and CH_3CHO has been investigated experimentally over the temperature and pressure range 29–107 K and 1.4–28.2 $\times$ 10^{16} molecules per cm^3, using a PLP-LIF technique. The low temperatures relevant to the ISM were achieved by a pulsed Laval nozzle expansion. Over the temperatures and pressures investigated, the reaction was shown to have a negative temperature dependence and a positive pressure dependence. Yields for the production of the CH_3CO product from the reaction were determined at 67.1 and 35.0 K, by monitoring the production of OH from the reaction of CH_3CO with O_2. The full

PES for the NH_2 + CH_3CHO system was determined using electronic structure calculations, and these combined with RRKM theory to obtain rate coefficients and branching ratios over a broad range of temperatures and pressures. The calculated rate coefficients have been shown to be sensitive to the inclusion of hindered rotor (HR) potentials in the rate theory calculations. In particular, the magnitude and shape of the HR potentials for the PRCs have been shown to have a strong effect on the calculated density of states of the PRCs, and as such the calculated rate coefficients are sensitive to this. Species time profiles produced by these calculations indicate that on the timescales of our experiments, the loss of NH_2 we observe is primarily due to the formation of the PRCs, and in particular PRC2, which on timescales significantly longer than our experiments will go on to form products (both channels (R1a) and (R1b)). However, as observed in our experiments, some CH_3CO is formed on the same timescale as NH_2 is lost; this instant CH_3CO can be thought of as the CH_3CO produced from well-skipping, and is sensitive to the height of the acetyl H-abstraction transition state (TS1). The experimentally determined rate coefficients and yields have been used to fit the calculated PES, from which low-pressure liming rate coefficients relevant to the ISM have been determined. These low-pressure limiting rate coefficients have been included in a single point dark cloud astronomical model, in which the reaction is shown to be a potential source of CH_3CO radicals under dark cloud conditions.

Conflicts of interest

There are no conflicts to declare.

Acknowledgements

We are grateful for the Science and Technology Facilities Council (STFC) for funding of this work under grant number ST/T000287/1. CW further acknowledges financial support from UKRI research and innovation grant number MR/T040726/1.

References

1 E. Herbst and E. F. van Dishoeck, Complex Organic Interstellar Molecules, in *Annual Review of Astronomy and Astrophysics*, ed. R. Blandford, J. Kormendy and E. van Dishoeck, 2009, vol. 47, pp. 427–480.
2 B. A. McGuire, *Astrophys. J. Suppl.*, 2022, **259**, 30.
3 A. I. Vasyunin and E. Herbst, *Astrophys. J.*, 2013, **769**, 34.
4 S. A. Sandford, M. Nuevo, P. P. Bera and T. J. Lee, *Chem. Rev.*, 2020, **120**, 4616–4659.
5 K. Altwegg, H. Balsiger, A. Bar-Nun, J. J. Berthelier, A. Bieler, P. Bochsler, C. Briois, U. Calmonte, M. R. Combi, H. Cottin, *et al.*, *Sci. Adv.*, 2016, **2**, e1600285.
6 R. Saladino, C. Crestini, S. Pino, G. Costanzo and E. Di Mauro, *Phys. Life Rev.*, 2012, **9**, 84–104.
7 R. H. Rubin, G. W. Swenson, R. C. Benson, H. L. Tigelaar and W. H. Flygare, *Astrophys. J.*, 1971, **169**, L39.

8 J. M. Hollis, F. J. Lovas, A. J. Remijan, P. R. Jewell, V. V. Ilyushin and I. Kleiner, *Astrophys. J.*, 2006, **643**, L25–L28.
9 K. M. Douglas, D. I. Lucas, C. Walsh, N. A. West, M. A. Blitz and D. E. Heard, *Astrophys. J.*, 2022, **937**, L16.
10 S. E. Taylor, A. Goddard, M. A. Blitz, P. A. Cleary and D. E. Heard, *Phys. Chem. Chem. Phys.*, 2008, **10**, 422–437.
11 R. L. Caravan, R. J. Shannon, T. Lewis, M. A. Blitz and D. E. Heard, *J. Phys. Chem. A*, 2015, **119**, 7130–7137.
12 J. C. Gomez Martin, R. L. Caravan, M. A. Blitz, D. E. Heard and J. M. C. Plane, *J. Phys. Chem. A*, 2014, **118**, 2693–2701.
13 R. J. Shannon, M. A. Blitz, A. Goddard and D. E. Heard, *Nat. Chem.*, 2013, **5**, 745–749.
14 R. J. Shannon, R. L. Caravan, M. A. Blitz and D. E. Heard, *Phys. Chem. Chem. Phys.*, 2014, **16**, 3466–3478.
15 K. Douglas, M. A. Blitz, W. H. Feng, D. E. Heard, J. M. C. Plane, E. Slater, K. Willacy and P. W. Seakins, *Icarus*, 2018, **303**, 10–21.
16 K. M. Douglas, M. A. Blitz, W. Feng, D. E. Heard, J. M. C. Plane, H. Rashid and P. W. Seakins, *Icarus*, 2019, **321**, 752–766.
17 N. A. West, T. J. Millar, M. Van de Sande, E. Rutter, M. A. Blitz, L. Decin and D. E. Heard, *Astrophys. J.*, 2019, **885**, 134.
18 S. Bull, I. Seregrennaja and P. Tsherbakora, *Khim. Prom.*, 1963, **7**, 507–509.
19 R. A. Copeland, D. R. Crosley and G. P. Smith, In laser-induced fluorescence spectroscopy of NCO and NH_2 in atmospheric pressure flames, in *Symposium (International) on Combustion*, Elsevier, 1985, pp. 1195–1203.
20 V. M. Donnelly, A. P. Baronavski and J. R. McDonald, *Chem. Phys.*, 1979, **43**, 271–281.
21 K. Yamasaki, A. Watanabe, T. Kakuda, A. Itakura, H. Fukushima, M. Endo, C. Maruyama and I. Tokue, *J. Phys. Chem. A*, 2002, **106**, 7728–7735.
22 P. Limão-Vieira, S. Eden, N. J. Mason and S. V. Hoffmann, *Chem. Phys. Lett.*, 2003, **376**, 737–747.
23 M. J. Frisch, G. W. Trucks, H. B. Schlegel, G. E. Scuseria, M. A. Robb, J. R. Cheeseman, G. Scalmani, V. Barone, B. Mennucci, G. A. Petersson, *et al.*, *Gaussian 09, Revision D.01*, Gaussian, Inc., Wallingford, CT, 2013.
24 T. H. Dunning Jr, *J. Chem. Phys.*, 1989, **90**, 1007–1023.
25 R. A. Kendall, T. H. Dunning Jr and R. J. Harrison, *J. Chem. Phys.*, 1992, **96**, 6796–6806.
26 D. E. Woon and T. H. Dunning Jr, *J. Chem. Phys.*, 1995, **103**, 4572–4585.
27 Y. Zhao and D. G. Truhlar, *Theor. Chem. Acc.*, 2008, **120**, 215–241.
28 NIST Computational Chemistry Comparison and Benchmark Database, **http://cccbdb.nist.gov/**.
29 R. J. Bartlett and G. D. Purvis, *Int. J. Quantum Chem.*, 1978, **14**, 561–581.
30 J. A. Pople, R. Krishnan, H. B. Schlegel and J. S. Binkley, *Int. J. Quantum Chem.*, 1978, **14**, 545–560.
31 D. R. Glowacki, C.-H. Liang, C. Morley, M. J. Pilling and S. H. Robertson, *J. Phys. Chem. A*, 2012, **116**, 9545–9560.
32 K. H. Gericke, L. M. Torres and W. A. Guillory, *J. Chem. Phys.*, 1984, **80**, 6134–6140.
33 T.-X. Xiang, K.-H. Gericke, L. M. Torres and W. A. Guillory, *Chem. Phys.*, 1986, **101**, 157–163.

34 W. Hack, H. Kurzke, P. Rouveirolles and H. G. Wagner, *Ber. Bunsen-Ges. Phys. Chem.*, 1986, **90**, 1210–1219.
35 S. Blazquez, D. Gonzalez, E. M. Neeman, B. Ballesteros, M. Agundez, A. Canosa, J. Albaladejo, J. Cernicharo and E. Jimenez, *Phys. Chem. Chem. Phys.*, 2020, **22**, 20562–20572.
36 D. H. Jaffer and I. W. M. Smith, *Faraday Discuss. Chem. Soc.*, 1979, **67**, 212–220.
37 M. Quack and J. Troe, *Ber. Bunsen-Ges. Phys. Chem.*, 1975, **79**, 170–183.
38 R. A. Copeland, D. R. Crosley and G. P. Smith, *Symp. (Int.) Combust., [Proc.]*, 1985, **20**, 1195–1203.
39 N. U. M. Howes, J. P. A. Lockhart, M. A. Blitz, S. A. Carr, M. T. Baeza-Romero, D. E. Heard, R. J. Shannon, P. W. Seakins and T. Varga, *Phys. Chem. Chem. Phys.*, 2016, **18**, 26423–26433.
40 L. Onel, L. Thonger, M. A. Blitz, P. W. Seakins, A. J. C. Bunkan, M. Solimannejad and C. J. Nielsen, *J. Phys. Chem. A*, 2013, **117**, 10736–10745.
41 V. Barone, C. Latouche, D. Skouteris, F. Vazart, N. Balucani, C. Ceccarelli and B. Lefloch, *Mon. Not. R. Astron. Soc.: Lett.*, 2015, **453**, L31–L35.
42 Q. S. Li and R. H. Lü, *J. Phys. Chem. A*, 2002, **106**, 9446–9450.
43 L. Song and J. Kästner, *Phys. Chem. Chem. Phys.*, 2016, **18**, 29278–29285.
44 F. Vazart, D. Calderini, C. Puzzarini, D. Skouteris and V. Barone, *J. Chem. Theory Comput.*, 2016, **12**, 5385–5397.
45 H. Keller-Rudek, G. K. Moortgat, R. Sander and R. Sörensen, *Earth System Science Data*, 2013, **5**, 365–373.
46 V. Wakelam, E. Herbst, J. C. Loison, I. W. M. Smith, V. Chandrasekaran, B. Pavone, N. G. Adams, M. C. Bacchus-Montabonel, A. Bergeat, K. Beroff, *et al.*, *Astrophys. J. Suppl.*, 2012, **199**, 21.
47 D. McElroy, C. Walsh, A. J. Markwick, M. A. Cordiner, K. Smith and T. J. Millar, *Astron. Astrophys.*, 2013, **550**, A36.
48 C. Walsh, H. Nomura and E. van Dishoeck, *Astron. Astrophys.*, 2015, **582**, A88.
49 J. Cernicharo, N. Marcelino, E. Roueff, M. Gerin, A. Jiménez-Escobar and G. M. Muñoz Caro, *Astrophys. J.*, 2012, **759**, L43.
50 I. Jiménez-Serra, A. I. Vasyunin, P. Caselli, N. Marcelino, N. Billot, S. Viti, L. Testi, C. Vastel, B. Lefloch and R. Bachiller, *Astrophys. J.*, 2016, **830**, L6.
51 A. Megías, I. Jiménez-Serra, J. Martín-Pintado, A. I. Vasyunin, S. Spezzano, P. Caselli, G. Cosentino and S. Viti, *Mon. Not. R. Astron. Soc.*, 2022, **519**, 1601–1617.
52 J.-C. Loison, M. Agúndez, N. Marcelino, V. Wakelam, K. M. Hickson, J. Cernicharo, M. Gerin, E. Roueff and M. Guélin, *Mon. Not. R. Astron. Soc.*, 2016, **456**, 4101–4110.
53 J.-C. Loison, M. Agúndez, V. Wakelam, E. Roueff, P. Gratier, N. Marcelino, D. N. Reyes, J. Cernicharo and M. Gerin, *Mon. Not. R. Astron. Soc.*, 2017, **470**, 4075–4088.